ACS APPLIED MATERIALS & INTERFACES

Research Article

Cite This: ACS Appl. Mater. Interfaces 2017, 9, 37136-37145

www.acsami.org

Multimaterial 3D Printing of Graphene-Based Electrodes for Electrochemical Energy Storage Using Thermoresponsive Inks

Victoria G. Rocha,*[,†,§] Esther García-Tuñón,*[,†,∥] Cristina Botas,[⊥] Foivos Markoulidis,[†,‡] Ezra Feilden,[†] Eleonora D'Elia,[†] Na Ni,[†] Milo Shaffer,[†,‡] and Eduardo Saiz[†]

[†]Department of Materials, Centre for Advanced Structural Ceramics and [‡]Department of Chemistry, Nanostructured Hierarchical Assemblies and Composites Group, Imperial College London, London SW7 2AZ, U.K.

[§]School of Engineering, Cardiff University, Cardiff CF24 3AA, U.K.

[∥]School of Engineering & Materials Innovation Factory, University of Liverpool, Liverpool L69 3GH, U.K.

[⊥]CIC Energigune, Parque Tecnológico de Álava, Albert Einstein 48, 01510 Miñano, Álava, Spain

Supporting Information

ABSTRACT: The current lifestyles, increasing population, and limited resources result in energy research being at the forefront of worldwide grand challenges, increasing the demand for sustainable and more efficient energy devices. In this context, additive manufacturing brings the possibility of making electrodes and electrical energy storage devices in any desired three-dimensional (3D) shape and dimensions, while preserving the multifunctional properties of the active materials in terms of surface area and conductivity. This paves the way to optimized and more efficient designs for energy devices. Here, we describe how three-dimensional (3D) printing will allow the fabrication of bespoke devices, with complex geometries, tailored to fit specific requirements and applications, by designing water-based thermoresponsive inks to 3D-print different materials in one step, for example, printing the active material precursor (reduced chemically modified graphene (rCMG)) and the current collector (copper) for supercapacitors or anodes for lithium-ion batteries. The formulation of thermoresponsive inks using Pluronic F127 provides an aqueous-based, robust, flexible, and easily upscalable approach. The devices are designed to provide low resistance interface, enhanced electrical properties, mechanical performance, packing of rCMG, and low active material density while facilitating the postprocessing of the multicomponent 3D-printed structures. The electrode materials are selected to match postprocessing conditions. The reduction of the active material (rCMG) and sintering of the current collector (Cu) take place simultaneously. The electrochemical performance of the rCMG-based self-standing binder-free electrode and the two materials coupled rCMG/Cu printed electrode prove the potential of multimaterial printing in energy applications.

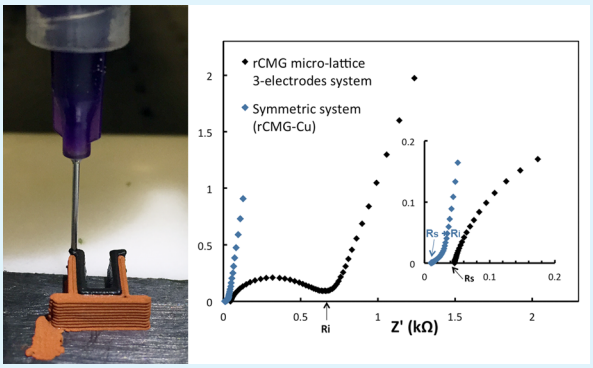

KEYWORDS: *graphene oxide, graphene-based devices, colloidal processing, additive manufacturing, 3D printing*

INTRODUCTION

Additive manufacturing (AM) technologies, based on making a three-dimensional (3D) object of virtually any shape from a digital model, open up completely new possibilities to design and fabricate devices and structures. AM promises integrated, customized, and unusually shaped components with improved performance that can be created on demand in a one-step process. On the other hand, graphene, with its unique intrinsic properties, is expected to revolutionize a wide range of applications, including membranes,[1] multifunctional composites,[2] Joule heaters,[3] supercapacitors,[4] Li-ion batteries (LIBs),[5] and redox-flow batteries,[6] among other energy applications.[7] The integration of graphene in AM is attracting increasing attention as a path to extend its practical applications.[8,9] This is particularly attractive in the context of electrodes and devices for electrical energy storage (EES).[10−13] Despite the continuous progress on graphene research and AM, there are still many issues to address, for example, combining graphene with other materials or retaining its unique intrinsic properties during the process.[14] Graphene, with a theoretical surface area of 2600 m^2 g^{-1}, high electrical conductivity, and mechanical robustness, has the potential to improve the performance of EES current devices. The current routes to prepare an electrode for an EES system show two main limitations.

First, they require a significant amount of binder (>5 wt %) to prepare slurries or inks that can be used to coat current-collecting foils that are then laminated into thin films and integrated into pouch, prismatic, or button cells. Their

Received: July 14, 2017
Accepted: September 18, 2017
Published: September 18, 2017

ACS Publications © 2017 American Chemical Society

DOI: 10.1021/acsami.7b10285
ACS Appl. Mater. Interfaces 2017, 9, 37136−37145

ACS Appl. Mater. Interfaces 2017.9:37136-37145.
Downloaded from pubs.acs.org by KAOHSIUNG MEDICAL UNIV on 09/27/18. For personal use only.

performance is hindered as the binder increases the electrical resistivity of the electrode. Conductive additives, such as carbon black or carbon nanotubes (CNTs),[15] are often used to mitigate these problems. A promising approach involves the preparation of aerogels based on binder-free graphene[16−18] or CNTs[19,20] as 3D seamless electrodes. A huge effort is currently being made on the wet processing of aerogels and 3D structures from graphene-related two-dimensional (2D) materials.[21,22]

Second, many EES devices show limited performance due to the thin-film configuration, which provides insufficient interfacial areas for energy storage. Recently direct ink writing (DIW) has been proved as an efficient way to integrate 2D materials and therefore increasing the interfacial area.[17,23,24] This AM technique enables 3D printing of any material that can be processed into a paste with optimized viscoelastic flow; it also allows building multimaterial 3D structures with fine resolution while minimizing waste.[25] One of the first EES devices using DIW consisted of an interdigitated micro-battery.[26] More recently, a full cell combining electrodes of graphene oxide (GO) and lithium iron phosphate ($LiFePO_4$) and lithium titanium oxide ($Li_4Ti_5O_{12}$) as cathode and anode materials was also made using DIW.[27] Both studies are examples of the potential of DIW in energy devices, but despite the rapid progress in this field, there are still fundamental challenges to overcome. It is necessary to provide more flexible, robust, and simple water-based approaches for multimaterial printing, avoiding complicated bespoke formulations and solvent-based systems.

In this work, we address the challenge of assembling 2D colloids of chemically modified graphene (CMG) with other materials to build multimaterial devices using an AM technique based on the continuous extrusion of colloidal inks at room temperature. This process enables the direct printing of electrodes for EES in any desired 3D shape and dimensions, while preserving the multifunctional properties of the active materials in terms of surface area and conductivity. The challenge is to formulate colloidal inks of different materials with matching flow behavior and viscoelasticity to manufacture multicomponent electrodes for EES applications. Here, we use an aqueous-based thermoresponsive formulation to fabricate proof-of-concept electrodes combining chemically modified graphene (CMG) as the active material and copper as current collector. Copper, a common current collector of anodes for LIBs, is selected as the archetypical example of a high-conductivity metallic track, whose sintering conditions match the thermal treatment required to reduce the CMG aerogels in the electrode. These formulations are water-based, nontoxic, flexible, and easily upscalable, facilitating the design of inks containing different materials (in terms of shape, size, chemistry, and surface area) from 2D materials (CMG) to metallic particles (Cu), with optimized rheological behavior to 3D-printed multimaterial devices.

EXPERIMENTAL METHODS

Materials. Spherical copper powder was purchased from Alfa Aesar, with an average particle size of 10 μm and purity of 99.9% (metals basis). Tens of grams of chemically modified graphene (CMG) were reproducibly and safely prepared using a modified procedure from Tour et al.,[28] using natural graphite powder, Aldrich (Supporting Information). Pluronic F127 powder, BioReagent, suitable for cell culture, was purchased from Sigma-Aldrich. Supercapacitor components: cellulose paper separator (TF4060; Nippon Kodoshi Corp.), "nanowhisker" Al foil tab (Toyal Carbo; Toyo Aluminium K.K.), and 1-ethyl-3-methylimidazolium bis-(trifluoromethylsulfonyl)imide (EMI-TFSI, 99%; Iolitec) electrolyte.

CMG Synthesis. CMG synthesis was performed in a custom-built reactor designed to manipulate up to 10 L of concentrated acids. In a typical synthesis, a 9:1 mixture of concentrated H_2SO_4/H_3PO_4 (3:0.3 L) was mixed with 24 g of natural graphite flakes (150−500 μm sieved; Aldrich), followed by the addition of 144 g of $KMnO_4$ (6 wt %). This slightly exothermic reaction increased the temperature up to 35−40 °C during the mixing process. Afterward, the temperature controller was set at 50 °C while stirring vigorously at 400 rpm for 18 h. Once completed, the reactor was cooled down to room temperature and a peristaltic pump was used for the slow addition of 1.72 L of aqueous H_2O_2 (2 wt %) that stopped the oxidation. The graphene oxide suspension was washed using repeated centrifugation at 9000 rpm (Thermo Scientific Sorvall LYNX 6000 super speed centrifuge) and redispersion in double-distilled water. The work-up was carried out until the supernatant water of the centrifuged CMG was close to pH 6, typically occurring after 16 washing cycles. Low speed (<1000 rpm) centrifugation cycles were performed to remove any unexfoliated graphite particles.

CMG Characterization. The lateral dimensions of the CMG flakes were measured using optical microscopy (Axio Scope A1; Zeiss). The CMG content in the slurry was estimated from freeze-dried CMG samples. Thermogravimetric analysis (TGA, TG 449 F1 Jupiter thermo-nanobalance; Netzsch) was performed to evaluate the presence of impurities by heating the freeze-dried GO up to 800 °C at 10 °C min^{-1} in air. The carbon content was verified by elemental analysis.

Pluronic Stock Solution Preparation. A Thinky ARE-250 Mixer was used to prepare a Pluronic F127 stock solution (25 wt %) that was stored in a fridge for 24 h to facilitate the mixing (below the transition temperature (~17 °C) for F127 solution where its viscosity is very low). Until the stock solution became transparent, a consecutive sequence of steps of 2 min mixing, 2 min defoaming, and 15 min cooling (below lower critical solution temperature (LCST)) are followed to obtain a homogeneous solution that is then ready to prepare the inks.

Ink Formulation. A 25 wt % Pluronic F127 aqueous stock solution was prepared using a Thinky ARE-250 Mixer in a sealed HDPE thick wall container. The copper ink was prepared using the F127 stock solution and copper powder with solid loading up to 85 wt % to achieve the desired rheological behavior. CMG inks have been prepared from freeze-dried CMG, with a fixed weight ratio of CMG/Pluronic F127 of 1:1. Cu powders and CMG flakes were mixed with F127 solutions in an ice bath prior to homogenization and defoaming with Thinky ARE-250. The final solid content of the CMG inks varied between 2.5 and 6 wt %. Cu inks were prepared by mixing 10 μm spherical Cu particles (up to 85 wt %) with a 25 wt % aqueous F127 stock solution. The inks were prepared at least 24 h beforehand to ensure stable rheological response.

Ink Rheology. The flow behavior and viscoelastic properties of the copper and CMG inks were measured in a Discovery Hybrid Rheometer (HR1; TA Instruments), with a parallel plate (Ø = 40 mm) and a solvent trap cover. The viscoelastic properties (G', G'') were assessed with strain and frequency sweeps, and the effect of the temperature was monitored with a temperature ramp. In detail, viscoelastic fingerprints and linear viscosity region were evaluated with stress-controlled amplitude sweeps at a fixed frequency of 396 rad s^{-1} and stress-controlled frequency sweeps at a fixed strain of 0.15%.

Printing. Copper and CMG inks were used to print a 3D object in a single step using a robotic deposition device (RoboCAD 3.0; 3-D inks, Stillwater, OK) on a 0.5 mm thickness graphite paper.

Postprocessing. The printed electrodes were frozen in liquid nitrogen and freeze-dried for 48 h (FreeZone 4.5; Labconco Corporation), followed by thermal reduction at 900 °C for 1 h under 10% H_2/90% Ar atmosphere.

Structural, Mechanical, and Electrochemical Characterization. Printed samples and devices were thoroughly characterized using Brunauer−Emmett−Teller (BET), field emission scanning electron microscopy (FESEM), Raman spectroscopy, X-ray photoelectron

DOI: 10.1021/acsami.7b10285
ACS Appl. Mater. Interfaces 2017, 9, 37136−37145

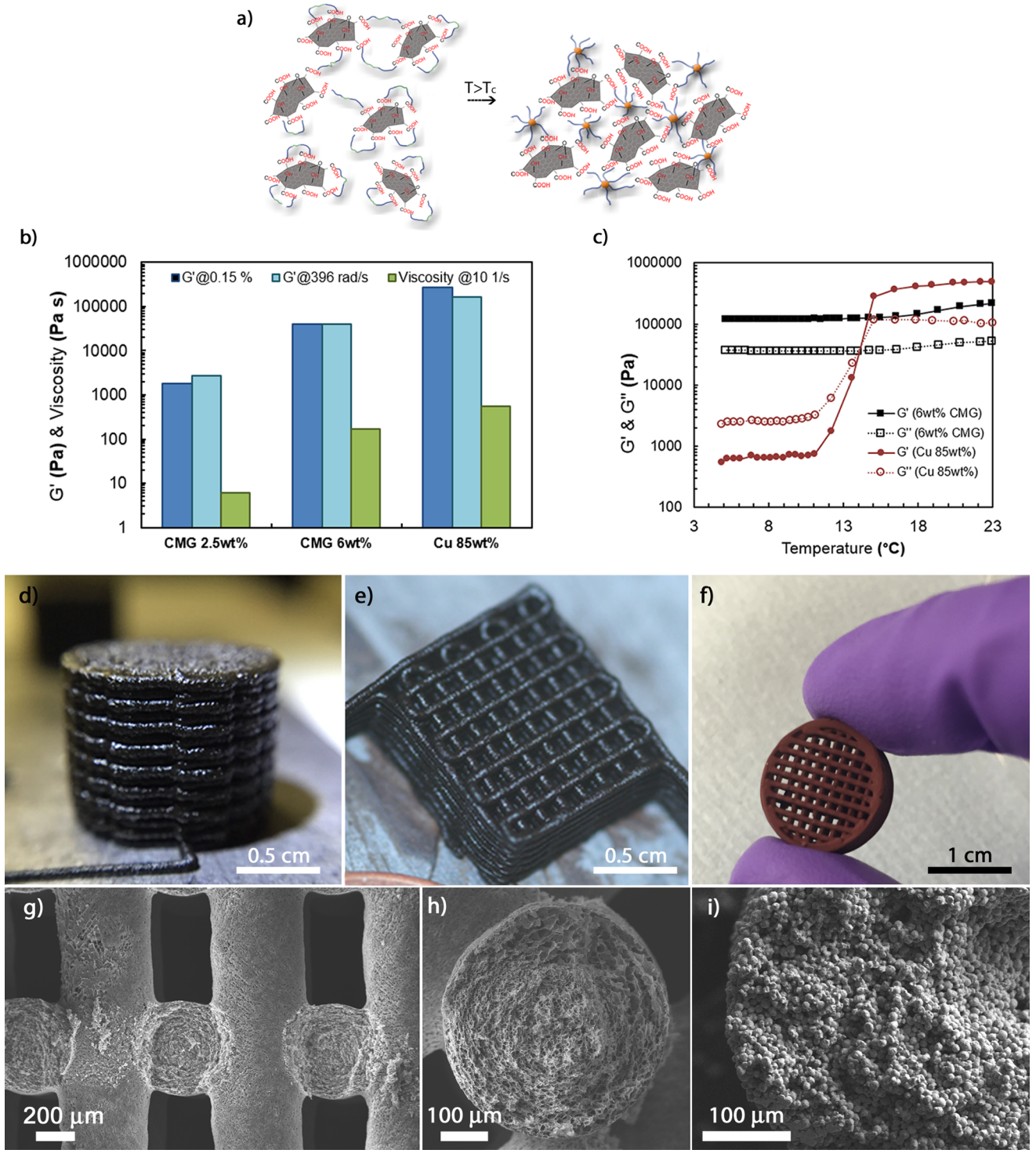

Figure 1. (a) Schematic illustration of the CMG assembly with a thermoresponsive nonionic triblock copolymer (CMG/F127 is 1:1). (b) Comparison of viscosity values and magnitude of the storage modulus (G' values obtained from two fingerprints: amplitude and frequency sweeps) for CMG (6 wt %) and Cu (85 wt %) water-based F127 inks. (c) Effect of temperature on viscoelasticity (temperature sweep) for CMG (6 wt %) and Cu (85 wt %) water-based F127 inks. (d–f) Images showing CMG and Cu 3D-printed structures: (d) CMG cylinder (Ø ~ 10 mm) made to characterize rCMG bulk properties (i.e., conductivity and mechanical behavior); (e) CMG grid designed for electrochemical testing; (f) Cu grid. (g–i) Images showing the internal microstructures after thermal reduction: (g) cross section of a woodpile CMG aerogel showing that the filaments are stiff enough to preserve their shape across gaps; (h, i) internal microstructures of the CMG (h) and Cu (i) filaments.

spectroscopy (XPS), transmission electron microscopy (TEM), and TGA as well as compression tests while monitoring their electrical conductivity.

Specific Surface. BET values were obtained using nitrogen physisorption at 77 K in 3 Flex (Micromeritics). The sample was degassed under vacuum for 16 h at 120 °C, followed by in situ degassing at 120 °C for 4 h. BET surface area calculation was obtained from the N_2 isotherm using 3 Flex version 3.02 software package (Micromeritics).

DOI: 10.1021/acsami.7b10285
ACS Appl. Mater. Interfaces 2017, 9, 37136–37145

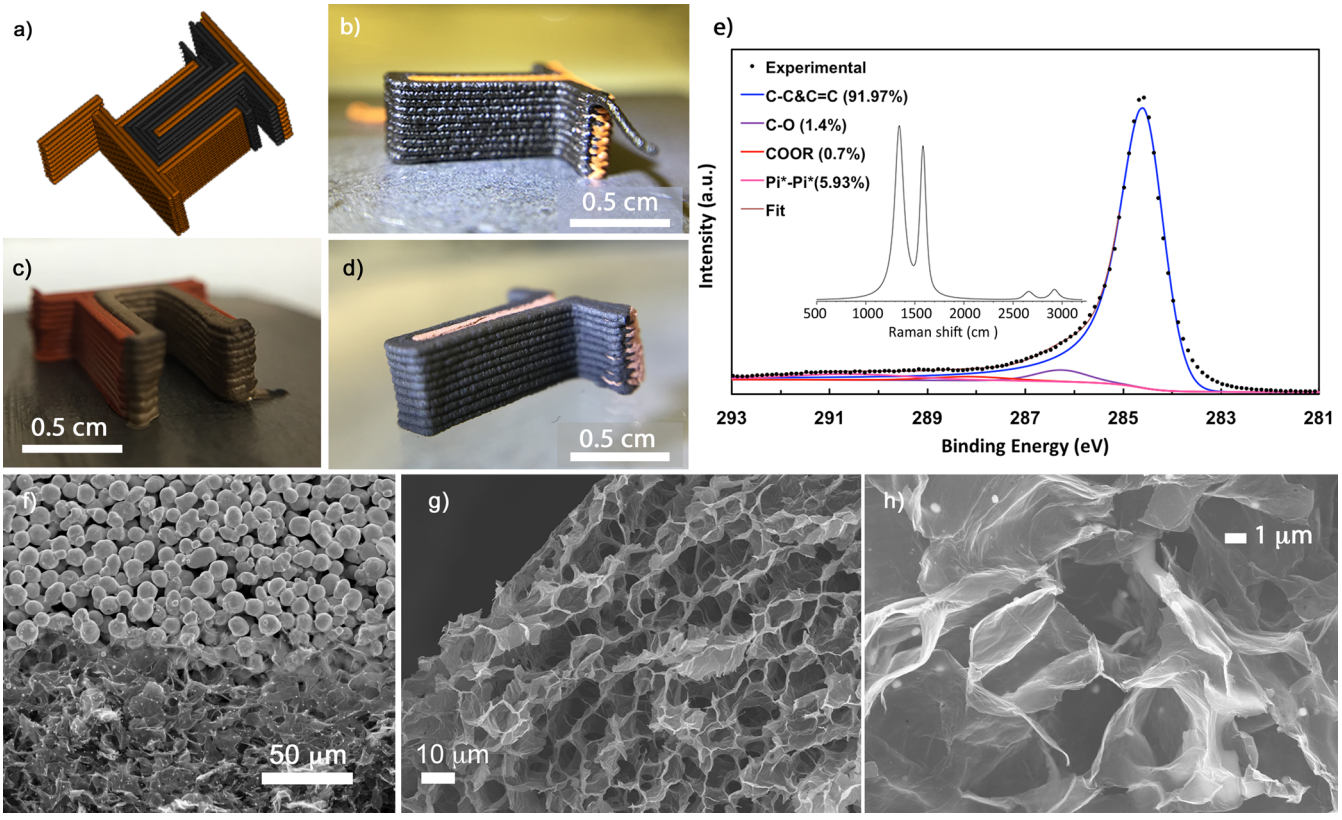

Figure 2. Three-dimensional-printed graphene-based electrodes. (a) Three-dimensional model for the printing process. The external walls of the electrode contain the current collector (two adjacent Cu lines), whereas the internal walls are made of the active material (two adjacent CMG lines). (b) Image of the as-printed CMG/Cu one-leg component showing the fine details of the piled up filaments extruded through the 500 μm nozzle using 6 wt % rCMG and 85 wt % Cu inks. (c) Two-leg electrode after freeze-drying and (d) one-leg component after simultaneous reduction (rCMG) and sintering (Cu) at 900 °C (same component as (b)). (e) XPS and Raman spectrum show the effective sp^2 recovery, after thermal treatment. FESEM images: (f) SEM images at the rCMG/Cu interface (g) and inside the rCMG filaments (h). At the Cu/rCMG interface, the flakes fully cover the surface of the Cu particles, showing very good physical contact. Cu nanospheres formed on the graphene flakes' surface were spotted throughout the active material, probably due to Cu evaporation and condensation. Copper does not wet carbon surfaces,[40] so it is not surprising that vapor condenses to form spherical nanoparticles during thermal reduction.

CMG and reduced (rCMG) objects were also characterized by FESEM and XPS and their electrical conductivity by the four-point probe method.

Field Emission Gun Scanning Electron Microscopy (FEG-SEM). Structural features were analyzed at 5 kV with field emission scanning electron microscopy on a LEO Gemini 1525 FEGSEM equipped with an energy dispersive spectroscopy microprobe (INCA Sight, Oxford Instruments, U.K.). All samples were coated with a thin Cr layer before the observation.

Transmission Electron Microscopy (TEM) and Scanning TEM (STEM). TEM and STEM of the rCMG electrode flakes were carried out using an FEI Titan 80−300 S/TEM operated at 80 kV

X-ray Photoelectron Spectroscopy (XPS). Analyses were performed on dried CMG, 3D-printed CMG/Pluronic, and rCMG 3D-printed networks using a K-Alpha spectrometer (ThermoFisher Scientific, East Grinstead, U.K.). XPS spectra were acquired using a microfocused monochromatic Al Kα X-ray source ($h\upsilon$ = 1486.6 eV). An X-ray spot of ~400 × 800 μm^2 ellipse shape was used and three different areas were spotted. Core level C 1s, C_{KLL}, O 1s, N 1s, Mn 1s, S 2p, Na 1s spectra were acquired using a pass energy of 200 eV and high regions at 40 eV.

XPS Data Analysis. Casa XPS was used for data interpretation. Shirley or two-point linear background subtractions were employed depending on the background shape. Scofield cross sections were used as relative sensitivity factors (RSFs) in the calculation of the atomic percentages (with RSF of C 1s = 1.000). Peaks were fitted using GL(30) lineshapes; a combination of Gaussian (70%) and Lorentzian (30%) shapes. All XP spectra were charge-corrected by referencing the fitted contribution of the C−C graphitic-like carbon in the C 1s signal to 284.6 eV. The atomic percentages were calculated from the peak areas in the acquired high-resolution C 1s and O 1s photoelectron spectra using Scofield sensitivity factors.

Raman Spectra. Raman spectra were recorded with a Renishaw Raman inVia microscope using a 532 nm excitation laser source at a laser power of 1.5 mW. The spectra were collected over an area of 25 × 25 μm^2, and an average spectrum was calculated.

Mechanical Characterization. The mechanical tests were carried out in a Zwick universal testing machine with a maximum load of 2 kN. The 3D structures were subjected to cyclic compression in the direction perpendicular to the printing plane: up to five cycles at 10 and 20% strain, with a holding period of 30 s under position-controlled movement of 1 mm min^{-1}.

Electrical Conductivity. A standard four-point probe method was used for conductivity measurements. The current was generated via a bench top power supply unit and kept at a constant direct current (DC) of 10 mA. Two electrodes were placed through the sample at a constant distance to monitor the voltage drop through the sample. The results were derived via standard equations for electrical conductivity and resistivity in DC.

Electrochemical Characterization. Electrochemical impedance spectroscopy (EIS) and Cyclic voltammetry (CV) were carried out using a Reference 600 Potentiostat/Galvanostat/ZRA, Gamry Instruments, Inc. Data analysis and fitting were completed using the Gamry Framework, EChem Analyst. Electrochemical tests in EMI-TFSI were performed using the following setups, assembled under nitrogen atmosphere:

DOI: 10.1021/acsami.7b10285
ACS Appl. Mater. Interfaces 2017, 9, 37136−37145

(i) Three-electrode system: rCMG (rectangular grid, dimensions: 5.0, 4.8, and 3.4 mm, Figure 1e) was used as the working electrode, silver wire as the counter electrode, and Ag/AgCl (3M NaCl) as the reference electrode (Figure S7). (ii) Pouch cell: symmetric double-layer capacitor (EDLC) with 3D-printed rCMG/Cu-based samples as electrodes and cellulose paper as a separator (Figure 3). Further details and protocols can be found in the Supporting Information.

RESULTS AND DISCUSSION

Ink Formulation, Rheology, and Printing. The colloidal inks are based on a commercially available thermoresponsive polymer (Pluronic F127; BASF). F127 in water forms a hydrogel able to carry any particle system, such as ceramics with different compositions and particle shapes.[29,30] F127 is a triblock nonionic copolymer (poly(ethylene oxide)−poly(propylene oxide)−poly(ethylene oxide) (PEO−PPO−PEO)) that in solution responds to temperature by changing its configuration and as a consequence its flow and viscoelastic behavior. At temperatures below the lower critical solution temperature (<LCST), all three components in the triblock are hydrophilic and its viscosity is very low. At temperatures above its LCST, PPO becomes hydrophobic, leading to a change in the triblock conformation, with the formation of micelles that considerable increase viscosity. These hydrogels are a very versatile and robust carrier for controlling the flow and viscoelasticity of most materials. Inks with a wide range of solid contents are formulated by mixing CMG (Figure S1, Supporting Information) or Cu powders with F127 water solutions at a temperature of ∼4 °C (well below the LCST of ∼17 °C, Figure 1a). At room temperature (>LCST), the CMG flakes and F127 micelles assemble into a network, forming a soft solid with high viscosity and elastic behavior (Figure 1a−c). The oxygen functionalities distributed in the edges and surface of CMG flakes facilitate multiple F127−CMG interactions, leading to an assembled network. We propose the following mechanism: at temperatures below LCST, the PEO components in F127 triblocks may establish hydrogen bonds with carboxyl and hydroxyl functional groups in edges and basal planes in CMG. When the temperature rises over the LCST (between 15 and 19 °C for Cu and CMG inks with different solid and F127 concentrations, Figure 1c), the central part in the triblock (poly(propylene oxide) (PPO)) becomes hydrophobic. This results in the formation of hydrogel micelles and in hydrophobic interactions of the PPO segment with the unoxidized aromatic islands on the basal plane of CMG flakes.[31,32] These 3D assemblies result in soft solids with very flexible rheology, depending on the CMG content (Figure 1). Inks with concentrations between 2 and 6 wt % prepared from freeze-dried CMG (CMG/F127, 1:1 (dry weight)) display good viscoelastic flow for DIW. Three-dimensional structures with very different shapes and sizes (Figure 1d−f) were built following a computer design in a robocaster, using nozzles with diameters ranging from 1000 μm down to 100 μm, at printing speeds between 6 and 12 mm s^{-1}.

The inks are shear thinning with viscosity and storage modulus (G') that increase with CMG concentration (Figure 1b). They flow smoothly under shear and rapidly recover their initial stiffness as the shear decreases. These inks can be printed on demand in the shape of cylinders (Figure 1d) for electrical and mechanical testing or grids (Figure 1f) for electrochemical and surface area characterization and also as an integrated device (Figure 2). Inks with lower concentrations (2.5 wt %) can be printed through the narrowest nozzles (100 μm) but the extruded filaments are not stiff enough ($G' \sim 2$ kPa) to avoid deflection across spans. The storage modulus of inks with a CMG concentration of 6 wt % can reach values up to 100 kPa (Figure 1b,c). The filaments extruded from these inks are strong enough to support their weight without deflection across spans up to 0.6 mm (Figure 1g). Once printed, they maintain their shape whilst supporting subsequent layers (Figure 1d,e). F127 has an important role in stabilizing the flakes within the ink, avoiding restacking and agglomeration[32,33] while creating a homogeneous noncovalent network. These bonds can break down easily (providing shear thinning flow) and quickly rebuild, facilitating the recovery of the initial viscosity and elastic response once deposited. XPS spectra of as-printed CMG−F127 cylinders before thermal reduction confirm the ink formulation chemistry, displaying an increase of intensity for the peaks corresponding to F127 functional groups (Figure S2, Supporting Information).

Copper inks (Cu content 85 wt %) were prepared following the same process. These metallic conductive inks are also shear thinning and display a strong elastic behavior at temperatures above LCST (Figure 1b,c); their viscosity and storage modulus values are higher than those of CMG inks (Figure 1b). These differences are due to the intrinsic characteristics of CMG flakes and Cu particles forming the networks (size, shape, surface area, and density). Monitoring the viscoelastic properties during a temperature ramp provides a comparison of the two inks (Figure 1c). Both have lower G' and G'' values when the temperature drops below the LCST and the F127 hydrogel network breaks down but with different behaviors and structures. The Cu ink behaves as a viscoelastic solid, but the temperature drop breaks the network down completely, leading to a liquidlike system ($G'' > G'$, Figure 1e). For the CMG ink, G' and G'' only drop slightly and the elastic component still dominates ($G' > G''$); this ink behaves like a gel. This can be explained by the arrangement of 2D CMG flakes with a high aspect ratio in a liquid crystal[34,22,35,36] and the small contribution of low amounts of F127 (only 6 wt %) to the overall stiffness.

At room temperature (>20 °C), both inks have optimal viscoelastic flow for the 3D printing process (Figure 1c). We have printed a multicomponent electrode using two printing nozzles per layer (Figure 2a and Video in the Supporting Information). The multicomponent design consists of two electrodes, the external walls contain the current collector, and the inner walls are made of the active material precursor (Figure 2a−d). Using the same F127 formulation facilitates bonding between the lines while avoiding additional binding agents. After printing, the electrodes are fast-frozen with liquid nitrogen, freeze-dried (Figure 2c), and thermally reduced (Figure 2d). The combination of printing and freezing templates the inner architecture of the CMG filaments. Extrusion through nozzles with long tips aligns the CMG flakes along parallel flow streamlines creating an axial arrangement[37] in the cross section (Figures 1h and 2g), whereas freezing avoids collapse, shrinkage, and restacking of the flakes, preserving a highly interconnected structure. FEGSEM images of the internal microstructure within the rCMG filaments evidence high macroporosity (∼5−10 μm), with a concentric orientation of the pores along the axial direction (Figures 1g,h and 2g). This arrangement has also been observed in ceramic inks[37] and composites.[38,39]

Postprocessing and Characterization. Thermal reduction of CMGs and sintering of copper particles take place

DOI: 10.1021/acsami.7b10285
ACS Appl. Mater. Interfaces 2017, 9, 37136−37145

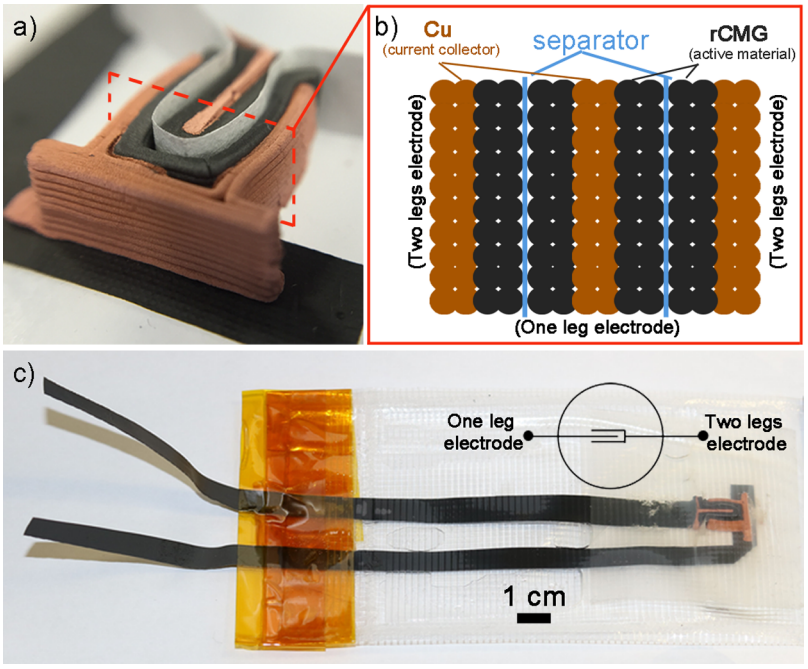

Figure 3. (a) Image of mounted supercapacitor device components prior to testing; including cellulose paper separator and positive and negative electrodes. (b) Scheme of the cross section showing a model of the Cu and rCMG filaments and separator. (c) Mounted device ready for testing: image of the vacuum-sealed supercapacitor pouch cell with protruding Al foil tabs; the inset shows a simplified diagram of the system.

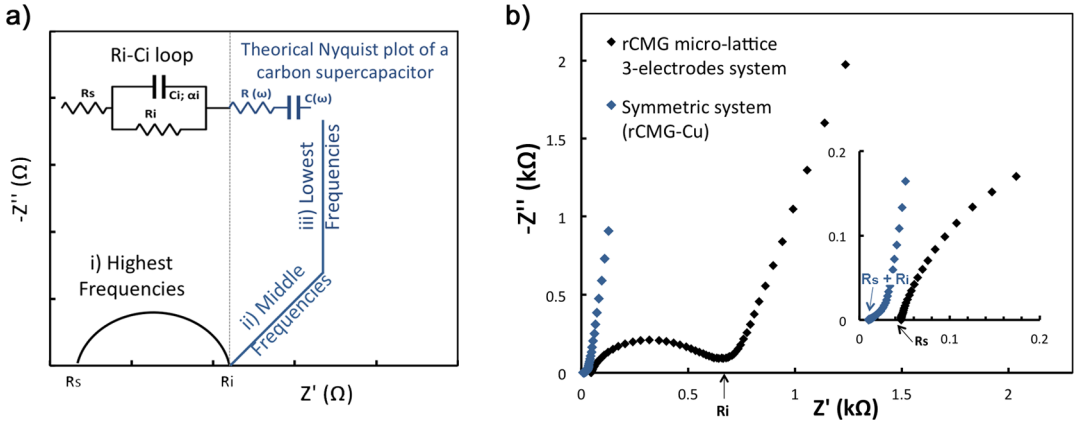

Figure 4. (a) Typical Nyquist plot of a carbon−carbon supercapacitor. It includes high to low frequency behavior of a supercapacitor with the equivalent circuits (R_s is the high frequency resistance, R_i the resistance of the active material/current collector interface, C_i the interface capacitance with the dispersion parameter α_i, $R(\omega)$ a part of the supercapacitor resistance depending on the frequency, and $C(\omega)$ the supercapacitor cell capacitance) and (b) Nyquist plots recorded from 100 kHz to 10 mHz, for the three-electrode (blue) and symmetric (black) systems in EMI-TFSI electrolyte, with their corresponding magnification of high and mid frequency response.

simultaneously. Cu particle size, shape, and solid loading are adjusted to match the shrinkage (~5% in volume) of the two materials during the thermal treatment. After reduction at 900 °C, we obtain a binder-free 3D structure consisting of a reduced graphene oxide (rGO) aerogel (rCMG) in direct contact with sintered copper (Figure 2d). Using the same formulation base and optimizing conditions to avoid mismatched shrinkage provided excellent contact between both materials (Figure 2f). The graphene oxide flakes cover the surface of the Cu particles, resulting in an interlocking interface between them. In fact, the presence of some sub-microparticles (<400 nm) of copper in the rCMG can also be observed due to the diffusion of copper into the rCMG (Figure 2f,h). XPS and Raman prove the quality of the partially reduced CMG prepared with F127 and confirm that the thermal reduction is effective (Figure 2e). The C/O ratio increases from 2 to 30, the spectrum displays sharper D and G peaks and, more importantly, the appearance of a 305 cm^{-1} width 2D peak at 2653 cm^{-1} that is characteristic of rGO (Figures 2e and S3c, Supporting Information). The reduction of 3D-printed CMG cylinders leads to aerogels with a bulk density of ~30 mg cm^{-3}, a BET surface area of 193 ± 2 m^2 g^{-1} (Figure S4), and electrical conductivity values of 90 ± 20 S m^{-1}. These values are comparable to those measured for other CMG-derived aerogels and printed structures.[17,41] The interconnected porous architecture on the microscale favors the flow of the electrolyte across the 3D network of active material thus facilitating ion transport. BET and TEM (Figure S5, Supporting Information) confirm the presence of mesopores (2−50 nm) that are considered beneficial for supercapacitor devices.[42]

DOI: 10.1021/acsami.7b10285
ACS Appl. Mater. Interfaces 2017, 9, 37136−37145

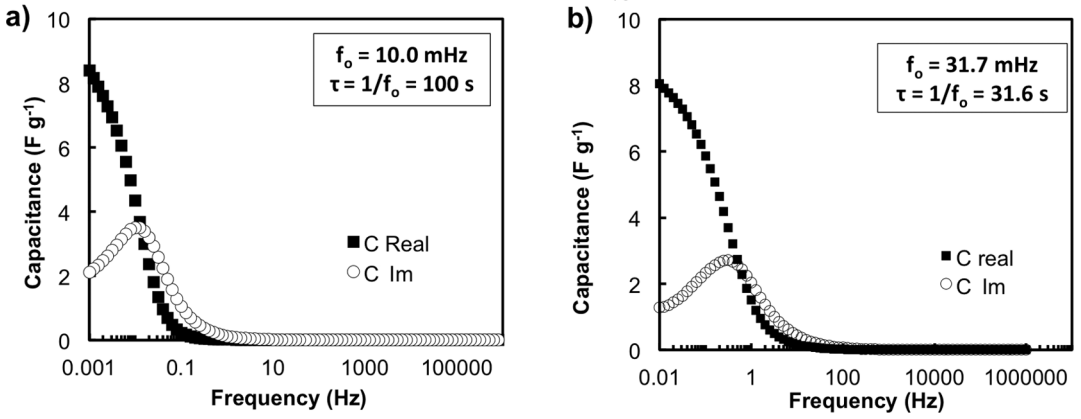

Figure 5. Imaginary (C_{im}) and real (C_{real}) parts of the capacitance plotted vs frequency (logarithmic scale) calculated from EIS results for the (a) three-electrode and (b) symmetric system, in EMI-TFSI electrolyte at 0 V, and their relaxation times (τ), which correspond to the inverse of the frequency at the maximum of C_{im} curves (f_0).

Cyclic compression tests were coupled with electrical conductivity measurements on 3D-printed rCMG cylinders; they show elastic−brittle behavior with strengths similar to other aerogels with similar densities.[43] During compression, they initially exhibit reversible elastic behavior (up to 10% strain) with consistent conductivity values after the second cycle (Figure S6, Supporting Information). Increasing the compression strain above 10% results in a change of the stress−strain slope due to "yielding" and microcracking at 18−20% that leads to a slight drop in conductivity values.

ELECTROCHEMICAL CHARACTERIZATION

Cyclic voltammetry (CV) of the three-electrode system using an ionic liquid (IL) (EMI-TFSI), selected as electrolyte because of the wide electrochemical stability window of ionic liquids (ILs) (energy density is directly proportional to the voltage squared),[44] stability to 3 V (Figure S8). The specific capacitance of the rCMG self-supporting electrodes calculated from the CVs is 16 F g^{-1} at 2 mV s^{-1} (Supporting Information). Additionally, the symmetric configuration, using two coupled multimaterial printed electrodes mounted as a symmetrical supercapacitor (Figure 3), demonstrates the potential of this approach to manufacture bespoke energy storage devices (Figures 3−6).

Electrochemical impedance spectroscopy (EIS) has been previously used to analyze the performance of devices, for example, to differentiate between the resistance and the capacitance of a supercapacitor.[45−47] The key plot of EIS measurements is the Nyquist plot, which represents the imaginary part of the impedance ($-Z_{im}$) versus the real part (Z_{real}). Z_{real} is related to the resistance of the electrolyte, the electrode, the contacts, and any other Faradaic resistance; Z_{im} is related to the charge storage mechanism and the reaction controlled by diffusion of the electrolyte.[48] From the generated Nyquist plots, it is possible to deduce many features related to the resistance (illustrated in Figure 4a).[46,47] The schematic representation has three different regions: (i) semicircle (high frequencies), (ii) 45° line (medium frequencies), and (iii) vertical line (low frequencies) (Figure 4a).

(i) The bulk electrolyte resistance, R_s, (the current collector could also be included[49]) can be identified at high frequencies (>1 kHz) from the generated Nyquist plots (Figure 4). The electrolyte and electrode compositions were the same for both configurations, but R_s is 5 times higher for the three-electrode system than for the symmetric one (64 and 13 Ω respectively) could be due to the smaller resistance of its current collector. The semicircle loop is also observed at high frequencies (defined as an resistor−capacitor (RC) circuit (R_i−C_i)) for the three-electrode system (Figure 4b).[46] This is related to the double-layer capacitance and charge-transfer resistance[49] (Figure 4a). C_i represents the interfacial capacitance at the interface, and α_i ($0 < \alpha_i < 1$) illustrates the nonideal behavior of C_i. When R_i tends to infinite, the interface is blocked and the cell works like a dielectric capacitor; when it tends to 0, the RC loop disappears and the Nyquist plot has the same shape as that of the ideal supercapacitor (Figure 4a). Generally, $R_s + R_i$ decreases if the electrolyte conductivity is increased or the resistivity of the interface of current collector−carbon electrode is decreased.[46,47] For the symmetric system, the Nyquist plot does not display the semicircle loop (Figure 4b) and R_i tends to a very low value. The same electrolyte is used in both configurations, but the total impedance for the multimaterial printed device (symmetric system) is significantly lower, demonstrating the good contact between the rCMG electrode and the copper current collector (Figure 2f). These results prove that printing both components (electrode and current collector) together favors the electronic contact between them.

(ii) The middle frequency region (45° line, Figure 4a) is due to the resistance depending on the frequency (R_ω); R_ω is associated with the electrolyte diffusion and penetration in the pores of the electrode.[45,47] For both systems, R_ω is small (Figure 4b) due to the large pores within the rCMG aerogel (Figure 2g).

(iii) At low frequency values (<1 kHz), the cell behavior is represented by the circuit $R_{sc}(\omega)$−$C(\omega)$ (Figure 4a), where $C(\omega)$ is the cell capacitance and $R_{sc}(\omega)$ the series resistance of the cell ($R_{sc}(\omega) = R_s + R_i + R_\omega$). $R_{sc}(\omega)$ depends on the impedance contact, and both of them vary with frequency. An ideal supercapacitor presents a vertical tail (Figure 4a); a nonvertical slope indicates that other processes (besides double-layer formation), such as diffusion limitations or Faradaic reactions,[45,49] might be taking place. In the Nyquist plots for both configurations,

DOI: 10.1021/acsami.7b10285
ACS Appl. Mater. Interfaces 2017, 9, 37136−37145

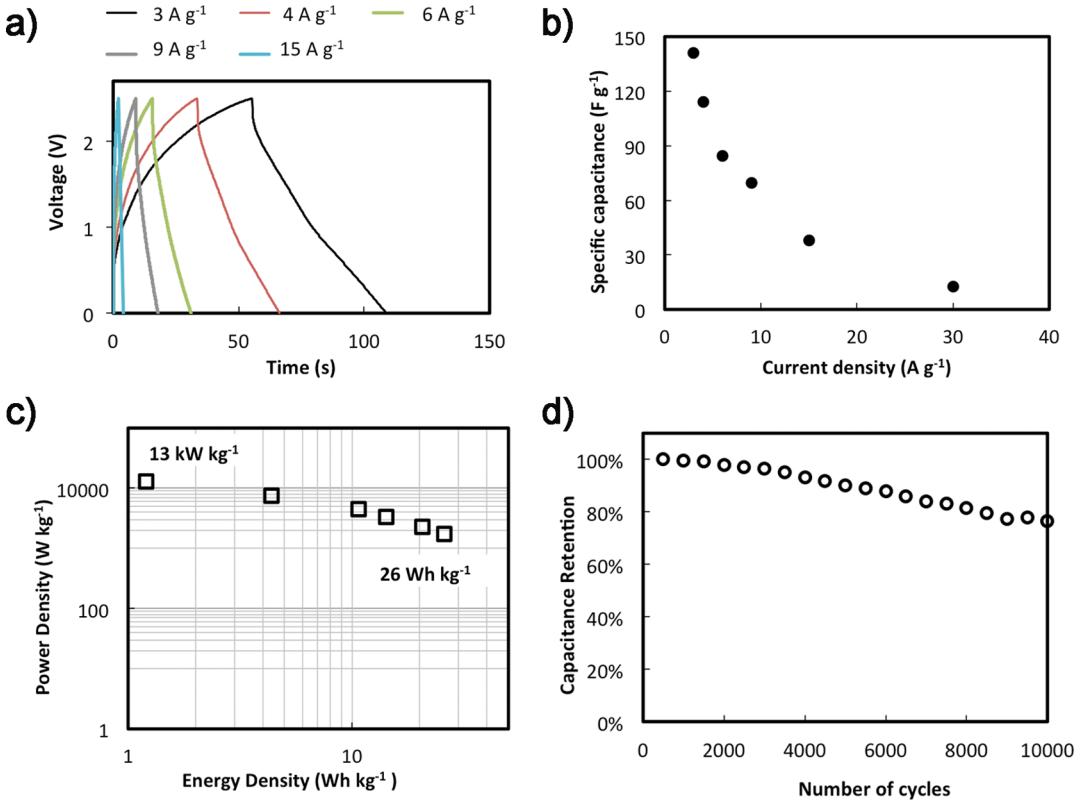

Figure 6. (a) Galvanostatic charge−discharge curves at increasing current densities for the symmetric device; (b) specific capacitance vs current density calculated from galvanostatic charge−discharge curves; (c) Ragone plot calculated from galvanostatic charge−discharge curves registered considering only the mass of the two electrodes of the supercapacitor device; and (d) cycle performance at 15 A g^{-1} for 10 000 cycles.

the tails are slightly tilted (Figure 4b) likely due to the high viscosity of the IL at room temperature.

From the EIS results, it is also possible to calculate the total effective capacitance of the cell and the relaxation time (τ, or time required to discharge half of the energy stored in the device) using eqs 1 and 2, respectively[47]

$$C(\omega) = C_{real}(\omega) - jC_{im}(\omega) = \frac{-Z_{im}(\omega)}{\omega |Z(\omega)|^2} - j\frac{Z_{real}(\omega)}{\omega |Z(\omega)|^2} \quad (1)$$

$$\tau_0 = \frac{1}{f_0} = \frac{2\pi}{\omega} \quad (2)$$

where j is the imaginary number, C_{real} the real part component of C and C_{im} the imaginary component, f_0 is the frequency reached at the maximum of C_{im}, and ω is the angular frequency.[48] The imaginary and real parts of the capacitance are plotted versus frequency (Figure 5).

The relaxation time is related to the ion diffusion, so the expected values for an IL are larger than those for aqueous electrolytes (<10 s); the value for the symmetric system is 31.6 s, which is 3 times smaller than that obtained for the three-electrode system due to the good electronic properties of the printed device.

The capacitance value calculated at a low frequency (close to the vertical line of the Nyquist Plot) is around 8 F g^{-1} (Figure 5). This is the expected value for an rCMG aerogel with a BET of 193 ± 2 m^2 g^{-1}, also in agreement with the results obtained by CVs (16 F g^{-1} at 2 mV s^{-1}, Figure S8) and with the galvanostatic charge−discharge curves (13 F g^{-1}) registered at high current density (30 A g^{-1}) for the symmetric system (Figure 6a,b). At lower current densities (3 A g^{-1}), the calculated capacitance increases up to 140 F g^{-1}, which could be attributed to redox reactions of the rCMG's residual oxygen functional groups (Figure 2e) or parasitic metal contamination. As a result, the specific energy and power densities reach values of 26 Wh kg^{-1} (at the power density of 1.7 kW kg^{-1}) and 13 kW kg^{-1} (at the energy density of 1.2 Wh kg^{-1}), respectively (Figure 6c). The capacitance retention at 15 A g^{-1} is rated 80% after 10 000 cycles (Figure 6d), indicating that the multi-material printed device has a promising viability and long-term stability. Optimization of the design and/or materials to improve the performance of the final device compared with other manufacturing approaches is beyond the scope of this proof of concept. Our results open up multiple possibilities, for example, in developing components for other energy devices, such as anodes for lithium-ion batteries, and the processing of carbon materials doped with nanoparticles or activated graphene (using chemical, hydrothermal, or physical activation) to enhance their initial surface area, and improve the capacitance (pseudocapacitance) of the final devices.

CONCLUSIONS

The formulation of thermoresponsive inks using F127 provides a robust, flexible, and easily upscalable approach to design and fabricate multicomponent graphene-based electrodes and devices for EES. They can be designed to provide enhanced mechanical performance, effective packing of rCMG, low active material density, and enhanced interface contact and electrical properties.

DOI: 10.1021/acsami.7b10285
ACS Appl. Mater. Interfaces 2017, 9, 37136−37145

This proof of concept demonstrates the capabilities of additive manufacturing techniques to make electrodes and devices for EES applications in bespoke configurations, which will eventually allow tailored designs that could be integrated in confined spaces. The thermoresponsive water-based hydrogel inks can be adapted to a broad range of materials from graphene to metals and ceramics, opening up new possibilities across disciplines, from EES devices to health and engineering; allowing the fabrication of customized devices tailored to fit applications with complex geometries. The formulations and strategy developed in this work will contribute to advance in the field of EES, in particular, in the fabrication of multimaterial supercapacitors, battery electrodes, and devices rationally designed to improve the interface between the materials and to optimize performance by decreasing the resistance of printed devices.

■ ASSOCIATED CONTENT

Supporting Information

The Supporting Information is available free of charge on the ACS Publications website at DOI: 10.1021/acsami.7b10285.

Extended methods for electrochemical characterization; BET characterization (PDF)

Cu/CMG electrode 3D printing (AVI)

■ AUTHOR INFORMATION

Corresponding Authors

*E-mail: GarciaRochaV@cardiff.ac.uk (V.G.R.).

*E-mail: Esther.GTunon@liverpool.ac.uk (E.G.-T.).

ORCID

Victoria G. Rocha: 0000-0001-6125-8556

Esther García-Tuñón: 0000-0001-9507-4501

Author Contributions

The manuscript was written through contributions of all authors. All authors have given approval to the final version of the manuscript.

Notes

The authors declare no competing financial interest.

■ ACKNOWLEDGMENTS

V.G.R. is grateful to the European Commission (FP7—Marie Curie Intra European Fellowship GRAPES). E.G.-T., E.S., and M.S. would like to acknowledge the EPSRC Grant graphene 3D networks (EP/K01658X/1). E.F. would like to acknowledge the CASC (Center for Advanced Structural Ceramics). N.N. would like to acknowledge the Junior Research Fellowship, Imperial College London. C.B. is grateful to the Spanish Government for the Jose Castillejo Mobility Grant (CAS15/00329) and the EU (Graphene Flagship Core 1). X-ray photoelectron spectra were obtained at the National EPSRC XPS Users' Service (NEXUS) at Newcastle University, an EPSRC Mid-Range Facility. The authors would like to acknowledge Dr. I. J.Villar-Garcia support on XPS data processing and analysis.

■ ABBREVIATIONS

PEO, poly(ethylene oxide); PPO, poly(propylene oxide)

■ REFERENCES

(1) Akbari, A.; Sheath, P.; Martin, S. T.; Shinde, D. B.; Shaibani, M.; Banerjee, P. C.; Tkacz, R.; Bhattacharyya, D.; Majumder, M. Large-Area Graphene-Based Nanofiltration Membranes by Shear Alignment of Discotic Nematic Liquid Crystals of Graphene Oxide. *Nat. Commun.* **2016**, No. 10891, DOI: 10.1038/ncomms10891.

(2) Singh, V.; Joung, D.; Zhai, L.; Das, S.; Khondaker, S. I.; Seal, S. Graphene Based Materials: Past, Present and Future. *Prog. Mater. Sci.* **2011**, *56*, 1178−1271.

(3) Yao, Y.; Fu, K. K.; Yan, C.; Dai, J.; Chen, Y.; Wang, Y.; Zhang, B.; Hitz, E.; Hu, L. Three-Dimensional Printable High-Temperature and High-Rate Heaters. *ACS Nano* **2016**, *10*, 5272−5279.

(4) Gu, W.; Yushin, G. Review of Nanostructured Carbon Materials for Electrochemical Capacitor Applications: Advantages and Limitations of Activated Carbon, Carbide-Derived Carbon, Zeolite-Templated Carbon, Carbon Aerogels, Carbon Nanotubes, Onion-Like Carbon, and Graphene. *Wiley Interdiscip. Rev.: Energy Environ.* **2014**, *3*, 424−473.

(5) Botas, C.; Carriazo, D.; Zhang, W.; Rojo, T.; Singh, G. Silicon-Reduced Graphene Oxide Self-Standing Composites Suitable as Binder-Free Anodes for Lithium-Ion Batteries. *ACS Appl. Mater. Interfaces* **2016**, *8*, 28800−28808.

(6) González, Z.; Botas, C.; Blanco, C.; Santamaría, R.; Granda, M.; Álvarez, P.; Menéndez, R. Thermally Reduced Graphite and Graphene Oxides in VRFBs. *Nano Energy* **2013**, *2*, 1322−1328.

(7) Quesnel, E.; Roux, F.; Emieux, F.; Faucherand, P.; Kymakis, E.; Volonakis, G.; Giustino, F.; Martín-García, B.; Moreels, I.; Gürsel, S. A.; Yurtcan, A. B.; Di Noto, V.; Talyzin, A.; Baburin, I.; Tranca, D.; Seifert, G.; Crema, L.; Speranza, G.; Tozzini, V.; Bondavalli, P.; Pognon, G.; Botas, C.; Carriazo, D.; Singh, G.; Rojo, T.; Kim, G.; Yu, W.; Grey, C. P.; Pellegrini, V. Graphene-Based Technologies for Energy Applications, Challenges and Perspectives. *2D Mater.* **2015**, *2*, No. 030204.

(8) Fu, K.; Yao, Y.; Dai, J.; Hu, L. Progress in 3D Printing of Carbon Materials for Energy-Related Applications. *Adv. Mater.* **2017**, *29*, No. 1603486.

(9) Ambrosi, A.; Pumera, M. 3D-Printing Technologies for Electrochemical Applications. *Chem. Soc. Rev.* **2016**, *45*, 2740−2755.

(10) Zhu, C.; Liu, T.; Qian, F.; Chen, W.; Chandrasekaran, S.; Yao, B.; Song, Y.; Duoss, E. B.; Kuntz, J. D.; Spadaccini, C. M.; Worsley, M. A.; Li, Y. 3D Printed Functional Nanomaterials for Electrochemical Energy Storage. *Nano Today* **2017**, 107.

(11) Wei, M.; Zhang, F.; Wang, W.; Alexandridis, P.; Zhou, C.; Wu, G. 3D Direct Writing Fabrication of Electrodes for Electrochemical Storage Devices. *J. Power Sources* **2017**, *354*, 134−147.

(12) Tian, X.; Jin, J.; Yuan, S.; Chua, C. K.; Tor, S. B.; Zhou, K. Emerging 3D-Printed Electrochemical Energy Storage Devices: A Critical Review. *Adv. Energy Mater.* **2017**, *7*, No. 1700127.

(13) Zhang, F.; Wei, M.; Viswanathan, V. V.; Swart, B.; Shao, Y.; Wu, G.; Zhou, C. 3D Printing Technologies for Electrochemical Energy Storage. *Nano Energy* **2017**, 418.

(14) Vlad, A.; Singh, N.; Galande, C.; Ajayan, P. M. Design Considerations for Unconventional Electrochemical Energy Storage Architectures. *Adv. Energy Mater.* **2015**, *5*, No. 1402115.

(15) Markoulidis, F.; Lei, C.; Lekakou, C.; Duff, D.; Khalil, S.; Martorana, B.; Cannavaro, I. A Method to Increase the Energy Density of Supercapacitor Cells by the Addition of Multiwall Carbon Nanotubes into Activated Carbon Electrodes. *Carbon* **2014**, *68*, 58−66.

(16) Zhu, C.; Han, T. Y.-J.; Duoss, E. B.; Golobic, A. M.; Kuntz, J. D.; Spadaccini, C. M.; Worsley, M. A. Highly Compressible 3D Periodic Graphene Aerogel Microlattices. *Nat. Commun.* **2015**, *6*, No. 6962.

(17) García-Tuñon, E.; Barg, S.; Franco, J.; Bell, R.; Eslava, S.; D'Elia, E.; Maher, R. C.; Guitian, F.; Saiz, E. Printing in Three Dimensions with Graphene. *Adv. Mater.* **2015**, *27*, 1688−1693.

(18) Jakus, A. E.; Secor, E. B.; Rutz, A. L.; Jordan, S. W.; Hersam, M. C.; Shah, R. N. Three-Dimensional Printing of High-Content Graphene Scaffolds for Electronic and Biomedical Applications. *ACS Nano* **2015**, *9*, 4636−4648.

(19) De Marco, M.; Markoulidis, F.; Menzel, R.; Bawaked, S. M.; Mokhtar, M.; Al-Thabaiti, S. A.; Basahel, S. N.; Shaffer, M. S. P. Cross-Linked Single-Walled Carbon Nanotube Aerogel Electrodes Via

Reductive Coupling Chemistry. *J. Mater. Chem. A* **2016**, *4*, 5385−5389.
(20) Worsley, M. A.; Merrill, M. D.; Charnvanichborikarn, S.; Kucheyev, S. O.; Satcher, J. H., Jr.; Stadermann, M.; Biener, J.; Baumann, T. F. Thick, Binder-Free Carbon-Nanotube-Based Electrodes for High Power Applications. *ECS J. Solid State Sci. Technol.* **2013**, *2*, M3140−M3144.
(21) Worsley, M. A.; Pham, T. T.; Yan, A. M.; Shin, S. J.; Lee, J. R. I.; Bagge-Hansen, M.; Mickelson, W.; Zettl, A. Synthesis and Characterization of Highly Crystalline Graphene Aerogels. *ACS Nano* **2014**, *8*, 11013−11022.
(22) Yao, B.; Chen, J.; Huang, L.; Zhou, Q.; Shi, G. Base-Induced Liquid Crystals of Graphene Oxide for Preparing Elastic Graphene Foams with Long-Range Ordered Microstructures. *Adv. Mater.* **2016**, *28*, 1623−1629.
(23) Li, W.; Li, Y.; Su, M.; An, B.; Liu, J.; Su, D.; Li, L.; Li, F.; Song, Y. Printing Assembly and Structural Regulation of Graphene Towards Three-Dimensional Flexible Micro-Supercapacitors. *J. Mater. Chem. A* **2017**, *5*, 16281−16288.
(24) Zhu, C.; Liu, T.; Qian, F.; Han, T. Y.-J.; Duoss, E. B.; Kuntz, J. D.; Spadaccini, C. M.; Worsley, M. A.; Li, Y. Supercapacitors Based on Three-Dimensional Hierarchical Graphene Aerogels with Periodic Macropores. *Nano Lett.* **2016**, *16*, 3448−3456.
(25) Smay, J. E.; Gratson, G. M.; Shepherd, R. F.; Cesarano, J.; Lewis, J. A. Directed Colloidal Assembly of 3D Periodic Structures. *Adv. Mater.* **2002**, *14*, 1279−1283.
(26) Sun, K.; Wei, T.-S.; Ahn, B. Y.; Seo, J. Y.; Dillon, S. J.; Lewis, J. A. 3D Printing of Interdigitated Li-Ion Microbattery Architectures. *Adv. Mater.* **2013**, *25*, 4539−4543.
(27) Fu, K.; Wang, Y.; Yan, C.; Yao, Y.; Chen, Y.; Dai, J.; Lacey, S.; Wang, Y.; Wan, J.; Li, T.; Wang, Z.; Xu, Y.; Hu, L. Graphene Oxide-Based Electrode Inks for 3D-Printed Lithium-Ion Batteries. *Adv. Mater.* **2016**, *28*, 2587−2594.
(28) Marcano, D. C.; Kosynkin, D. V.; Berlin, J. M.; Sinitskii, A.; Sun, Z.; Slesarev, A.; Alemany, L. B.; Lu, W.; Tour, J. M. Improved Synthesis of Graphene Oxide. *ACS Nano* **2010**, *4*, 4806−4814.
(29) Feilden, E.; Blanca, E. G.-T.; Giuliani, F.; Saiz, E.; Vandeperre, L. Robocasting of Structural Ceramic Parts with Hydrogel Inks. *J. Eur. Ceram. Soc.* **2016**, *36*, 2525−2533.
(30) Franco, J.; Hunger, P.; Launey, M. E.; Tomsia, A. P.; Saiz, E. Direct Write Assembly of Calcium Phosphate Scaffolds Using a Water-Based Hydrogel. *Acta Biomater.* **2010**, *6*, 218−228.
(31) Vasita, R.; Mani, G.; Agrawal, C. M.; Katti, D. S. Surface Hydrophilization of Electrospun PLGA Micro-/Nano-Fibers by Blending with Pluronic F-108. *Polymer* **2010**, *51*, 3706−3714.
(32) Zu, S.-Z.; Han, B.-H. Aqueous Dispersion of Graphene Sheets Stabilized by Pluronic Copolymers: Formation of Supramolecular Hydrogel. *J. Phys. Chem. C* **2009**, *113*, 13651−13657.
(33) Hong, B. J.; Compton, O. C.; An, Z.; Eryazici, I.; Nguyen, S. T. Successful Stabilization of Graphene Oxide in Electrolyte Solutions: Enhancement of Biofunctionalization and Cellular Uptake. *ACS Nano* **2012**, *6*, 63−73.
(34) Akbari, A.; Sheath, P.; Martin, S. T.; Shinde, D. B.; Shaibani, M.; Banerjee, P. C.; Tkacz, R.; Bhattacharyya, D.; Majumder, M. Large-Area Graphene-Based Nanofiltration Membranes by Shear Alignment of Discotic Nematic Liquid Crystals of Graphene Oxide. *Nat. Commun.* **2016**, *7*, No. 10891.
(35) Kim, J. E.; Han, T. H.; Lee, S. H.; Kim, J. Y.; Ahn, C. W.; Yun, J. M.; Kim, S. O. Graphene Oxide Liquid Crystals. *Angew. Chem., Int. Ed.* **2011**, *50*, 3043−3047.
(36) García-Tuñón, E.; Feilden, E.; Zheng, H.; D'Elia, E.; Leong, A.; Saiz, E. Graphene Oxide: An All-in-One Processing Additive for 3d Printing. *ACS Appl. Mater. Interfaces* **2017**, *9*, 32977−32989.
(37) Román-Manso, B.; Figueiredo, F. M.; Achiaga, B.; Barea, R.; Pérez-Coll, D.; Morelos-Gómez, A.; Terrones, M.; Osendi, M. I.; Belmonte, M.; Miranzo, P. Electrically Functional 3D-Architectured Graphene/SiC Composites. *Carbon* **2016**, *100*, 318−328.
(38) Román-Manso, B.; Chevillotte, Y.; Osendi, M. I.; Belmonte, M.; Miranzo, P. Thermal Conductivity of Silicon Carbide Composites with Highly Oriented Graphene Nanoplatelets. *J. Eur. Ceram. Soc.* **2016**, *36*, 3987−3993.
(39) Centeno, A.; Rocha, V. G.; Alonso, B.; Fernández, A.; Gutierrez-Gonzalez, C. F.; Torrecillas, R.; Zurutuza, A. Graphene for Tough and Electroconductive Alumina Ceramics. *J. Eur. Ceram. Soc.* **2013**, *33*, 3201−3210.
(40) Dezellus, O.; Eustathopoulos, N. The Role of Van Der Waals Interactions on Wetting and Adhesion in Metal Carbon Systems. *Scr. Mater.* **1999**, *40*, 1283−1288.
(41) Barg, S.; Perez, F. M.; Ni, N.; Pereira, P. d. V.; Maher, R. C.; Garcia-Tuñon, E.; Eslava, S.; Agnoli, S.; Mattevi, C.; Saiz, E. Mesoscale Assembly of Chemically Modified Graphene into Complex Cellular Networks. *Nat. Commun.* **2014**, *5*, No. 4328.
(42) Simon, P.; Gogotsi, Y. Materials for Electrochemical Capacitors. *Nat. Mater.* **2008**, *7*, 845−854.
(43) Ni, N.; Barg, S.; Garcia-Tunon, E.; Perez, F. M.; Miranda, M.; Lu, C.; Mattevi, C.; Saiz, E. Understanding Mechanical Response of Elastomeric Graphene Networks. *Sci. Rep.* **2015**, *5*, No. 13712.
(44) Peng, C.; Yang, L.; Fang, S.; Wang, J.; Zhang, Z.; Tachibana, K.; Yang, Y.; Zhao, S. Electrochemical Behavior of Copper Current Collector in Imidazolium-Based Ionic Liquid Electrolytes. *J. Appl. Electrochem.* **2010**, *40*, 653−662.
(45) Nian, Y.-R.; Teng, H. Influence of Surface Oxides on the Impedance Behavior of Carbon-based Electrochemical Capacitors. *J. Electroanal. Chem.* **2003**, *540*, 119−127.
(46) Portet, C.; Taberna, P. L.; Simon, P.; Laberty-Robert, C. Modification of Al Current Collector Surface by Sol−Gel Deposit for Carbon−Carbon Supercapacitor Applications. *Electrochim. Acta* **2004**, *49*, 905−912.
(47) Lewandowski, A.; Olejniczak, A.; Galinski, M.; Stepniak, I. Performance of Carbon−Carbon Supercapacitors Based on Organic, Aqueous and Ionic Liquid Electrolytes. *J. Power Sources* **2010**, *195*, 5814−5819.
(48) Yao, F.; Pham, D. T.; Lee, Y. H. Carbon-Based Materials for Lithium-Ion Batteries, Electrochemical Capacitors, and Their Hybrid Devices. *ChemSusChem* **2015**, *8*, 2284−2311.
(49) Béguin, F.; Frackowiak, E. *Supercapacitors: Materials, Systems, and Applications*; Wiley-VCH Verlag GmbH & Co. KGaA, 2013.

DOI: 10.1021/acsami.7b10285
ACS Appl. Mater. Interfaces 2017, 9, 37136−37145